Tidally Forced Internal Waves and Overturns Observed on a Slope: Results from HOME

MURRAY D. LEVINE AND TIMOTHY J. BOYD

College of Oceanic and Atmospheric Sciences, Oregon State University, Corvallis, Oregon

(Manuscript received 26 November 2004, in final form 11 August 2005)

ABSTRACT

Tidal mixing over a slope was explored using moored time series observations on Kaena Ridge extending northwest from Oahu, Hawaii, during the Survey component of the Hawaii Ocean Mixing Experiment (HOME). A mooring was instrumented to sample the velocity and density field of the lower 500 m of the water column to look for indirect evidence of tidally induced mixing and was deployed on a slope in 1453-m water depth for 2 months beginning in November 2000. The semidiurnal barotropic tidal currents at this site have a significant cross-ridge component, favorable for exciting an internal tidal response. A large-amplitude response is expected, given that the slope of the topography (4.5°) is nearly the same as the slope of the internal wave group velocity at semidiurnal frequency. Density overturns were inferred from temperature profiles measured every 2 min. The number and strength of the overturns are greater in the 200 m nearest the bottom, with overturns exceeding 24 m present at any depth nearly 10% of the time. Estimates of turbulent dissipation rate ε were made for each overturn by associating the measured Thorpe scale with the Ozmidov scale. The average ε between 1300 and 1450 m for the entire experiment is about 10^{-8} m^2 s^{-3}, corresponding to an average K_ρ of 10^{-3} m^2 s^{-1}. Both ε and K_ρ decrease by about an order of magnitude by 1200 m. The occurrence of overturns and the magnitude of ε are both highly correlated with the tide: both with the spring–neap cycle as well as the phase of the semidiurnal tide itself. Dissipation rate varies by at least an order of magnitude over the spring–neap cycle. It appears that tidal frequency vertical shear within 200 m of the boundary leads to significant strain (vertical divergence). Most of the overturns occur during the few hours when the vertical strain is greatest. The buoyancy frequency N calculated from reordering these overturns is a factor of 3 lower than the background $\overline{N}$. This is consistent with the following kinematic description: the internal tide first strains the mean density field, leading to regions of low N that subsequently overturn. Less regularly, overturns also occur when the internal tide strain has created relatively high stratification within 200 m of the bottom.

1. Introduction

The maintenance of the thermohaline structure in the ocean interior is a fundamental issue in physical oceanography. Munk (1966) suggested that the average vertical thermal structure could be explained as the result of a balance between the vertical upwelling of cold water subducted at the poles and the downward turbulent diffusion of heat from the upper ocean warmed by the sun. If this process occurs uniformly throughout the ocean, then a diapycnal diffusivity K_ρ of about 10^{-4} m^2 s^{-1} is needed. Decades of direct turbulence measurements, however, indicate an average diffusivity of order 10^{-5} m^2 s^{-1}—too weak to validate this hypothesis (e.g., Gregg 1989; Ledwell et al. 1993). One alternate hypothesis is that the mixing occurs over limited regions of steep topography, or "hot spots," rather than being distributed uniformly throughout the interior of the ocean (e.g., Armi 1978). This idea seems possible given the myriad possible nonlinear physical processes involving topography that could lead to the generation of turbulence.

Considering the energy source for mixing the deep ocean, recent calculations from global tidal models using the Ocean Topography Experiment (TOPEX) altimeter data suggest that the M_2 barotropic tide dissipates about 25%–30% of its total energy in the deep ocean (Egbert and Ray 2000, 2001). This result differs

Corresponding author address: Dr. Murray D. Levine, Oregon State University, 104 COAS Admin. Bldg., Corvallis, OR 97331. E-mail: levine@coas.oregonstate.edu

from the traditional view that almost all tidal dissipation in the ocean occurs in shallow seas. Using this new result, Munk and Wunsch (1998) reexamined the role of tidal energy in mixing the deep ocean and explored the many possible pathways that the conversion from barotropic tide to turbulence can follow. For example, tidal energy that ends up dissipated in deep topographic hot spots could result from directly forced motions that become unstable or from internal waves that rapidly become nonlinear and break. Undoubtedly, much of the energy lost from the barotropic tide in the deep ocean radiates away from the topography as low-mode internal tide (Merrifield and Holloway 2002). This energy is dissipated elsewhere and presumably does not contribute toward the creation of a hot spot of dissipation.

The Hawaii Ocean Mixing Experiment (HOME) was designed to study the importance of tidally induced mixing over steep topography (Pinkel et al. 2000). The Hawaiian Ridge was chosen as the experimental deep-water site because of a significant convergence of barotropic tidal energy flux in this region (Egbert and Ray 2000, 2001). During the first field component of HOME, known as the Survey experiment (September 2000–January 2001), indirect and direct measurements of the dissipation were made at various locations along the Hawaiian Ridge system. A broad spectrum of space and time scales were sampled using a wide variety of measurement techniques (Rudnick et al. 2003). The primary goals of this experiment were to validate the hypothesized enhanced mixing along the ridge and to identify a site for intensive sampling during the Nearfield experiment (August–November 2002). This paper reports on some results from the Survey experiment moored observations.

The moorings provide a temporal context to complement spatial surveys made by other investigators. The moorings were designed to resolve variability in velocity and density at tidal and higher frequencies within several hundred meters of the sloping bottom. Anticipating the generation of significant turbulence on the slope, temperature sensors were spaced on the mooring for the purpose of resolving large-scale overturns. Overturns provide evidence of instabilities and the generation of turbulence and can produce estimates of the dissipation rate of turbulent kinetic energy ε, using methods such as those described by Thorpe (1977).

The objective of this paper is to present a description of the gravitationally unstable overturns observed within the tidally varying velocity and density field over the bottom slope of the Hawaiian Ridge. The large barotropic tidal flow normal to the steep slope generates an internal tidal response. The number of overturns and the magnitude of ε estimated indirectly from the overturn structures are found to be highly correlated in time with the dominant semidiurnal tidal signal. Most of the overturns occur when the background stratification is reduced by the vertical strain of the internal tide. There is also significant correlation of the number of overturns with the spring–neap cycle of the tide, and ε varies by more than a factor of 10 over the fortnightly cycle. To fully understand the dynamics creating the observed overturns will require further theoretical and numerical modeling studies.

The experiment is described in section 2 along with the salient features of the mean temperature–salinity (T–S) relationship. The observed tidal flow is described and compared with a barotropic tidal model in section 3; a kinematically self-consistent description of the internal tidal response is also presented. Section 4 contains an analysis of the overturns as indicators of mixing. These results are compared with other observations of mixing near sloping topography in section 5. A summary and conclusions are provided in section 6.

2. Experimental description

As part of the HOME Survey experiment, two moorings were deployed in the Kauai Channel on the ridge extending northwest from Oahu, Hawaii, for 2 months beginning in November 2000 (Fig. 1). The data used in this analysis come from a variety of instruments on one of these moorings, named Big Boy, which was located on the north slope of the ridge at 21°48.00′N, 158°27.84′W in water depth of 1453 m (Boyd et al. 2002) (Fig. 2).

At the bottom of Big Boy an upward-looking 75-kHz acoustic Doppler current profiler (ADCP; manufactured by RDI, Inc.) measured velocity profiles every 8 min in 8-m vertical bins. The mean current speed over the 2-month deployment was less than 0.02 m s^{-1} at all depths. The range of the ADCP data was typically 200 m, increasing at times to over 400 m as a result of the diurnal variation in scattering strength. Some data were contaminated by the reflection of the acoustic beam sidelobes off sensors on the mooring, especially from sensors closer to the ADCP. Since the sensors are not moving, the effect of these reflections is to bias the measured speed at those ranges to lower values (D. Symonds, RDI, 2002, personal communication). This effect is mostly constrained to specific bins; hence, the data from these depths were not used in the analysis.

Temperature time series were recorded at 23 depths; conductivity was also measured at 5 of these depths (Fig. 2). A variety of instrumentation was used: 14 temperature recorders (Sea-Bird Electronics, SBE-39), 5 temperature–conductivity recorders (SBE-16), and 4

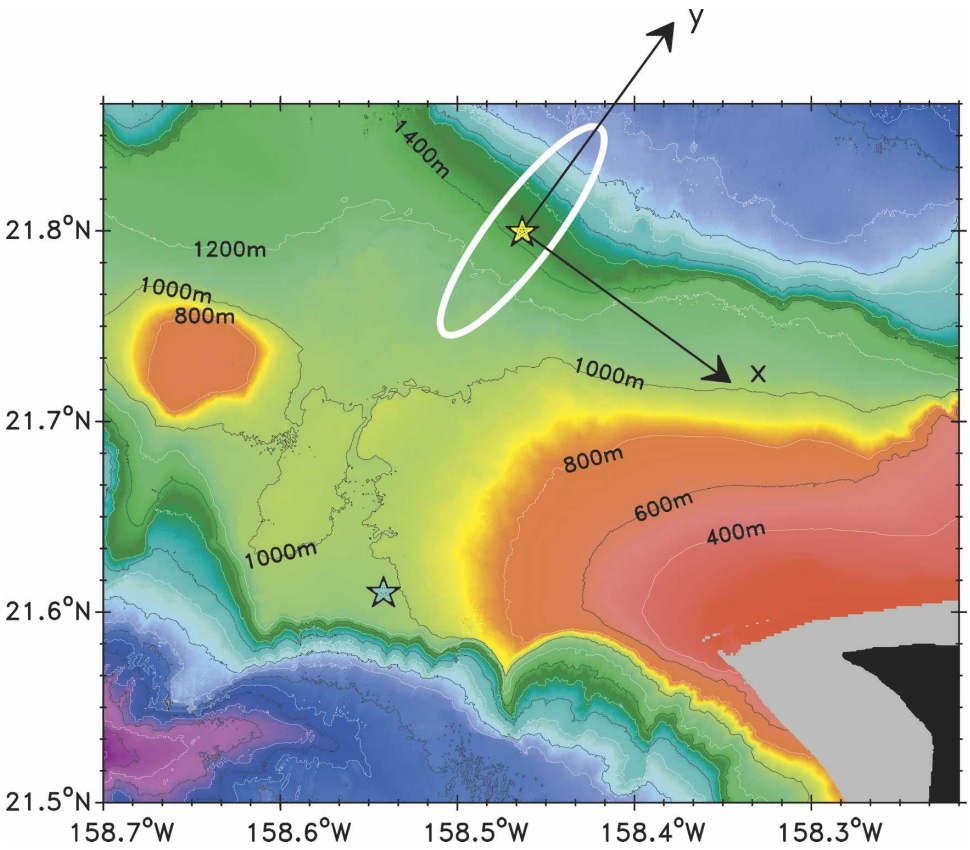

FIG. 1. Bathymetric contour plot of the ridge off northwest Oahu, HI. The location of the Big Boy (Shorty) mooring is indicated by a yellow (blue) star. The M_2 barotropic tidal ellipse is shown as estimated from the model of Egbert (1997); the maximum speed is 0.086 m s^{-1}. The (x, y) coordinate system defines the along-ridge and cross-ridge directions, respectively.

miniature temperature recorders [MTRs), produced by the National Oceanic and Atmospheric Administration/Pacific Marine Environmental Laboratory (NOAA/PMEL)]. The sampling rates were either 1 or 2 min, depending on the type of instrument. Temperature sensors were clustered in three vertical groups of seven instruments; sensors in each group were separated by 8 m to coincide with ADCP velocity bins. Conductivity was measured at the ends of the groups. The objective was to measure a *T–S* relationship that could be used to infer salinity, and hence density, within the groups at depths where only *T* was measured. Some additional sensors were placed between the groups to resolve variability at larger vertical scales. Only the deepest sensor was not spaced by a multiple of 8 m.

a. Temperature adjustment

Although the absolute temperature calibration was fairly accurate, it is important to have the best relative temperature calibration possible in order to resolve small vertical temperature gradients and inversions. All SBE sensors were calibrated at the factory before deployment, and the MTRs were calibrated in our Oregon State University (OSU) facility. The average observed *T* profile varied nearly linearly with depth over the 48 m within each group, with some small but obviously nonphysical deviations. To correct these deviations for this analysis, the average profiles were forced to be exactly linear over the 48 m by adding temperature offsets of order 0.001°C to the calibration. These slight adjustments to the calibration had minimal effect on the definition and analysis of overturns described below, since only the smaller, less energetic, overturns are affected.

b. T–S relationship

The average *T–S* relationship was estimated for each temperature–conductivity sensor using the potential temperature θ referenced to a pressure of 1300 dbar. Because of the large vertical advection, there is significant overlap in the range of the *T–S* curves measured at each instrument. The *T–S* curve for each sensor indi-

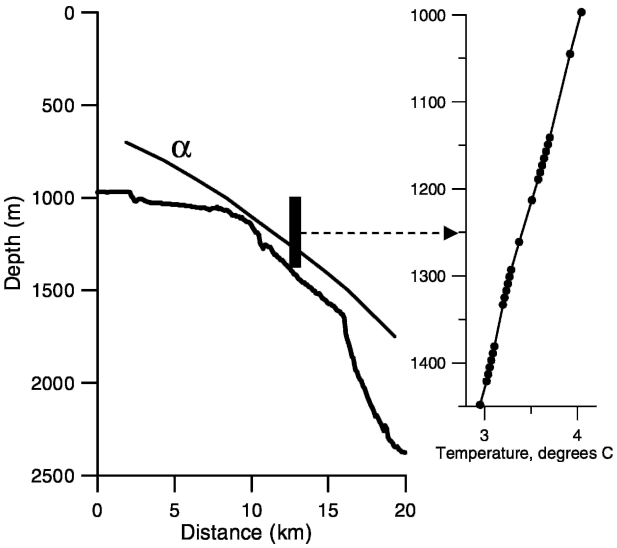

FIG. 2. Cross-ridge section of bottom topography showing location of mooring and the average temperature profile as measured by the moored sensors (dots). The slope α of the group velocity of an internal wave at semidiurnal tidal frequency is also shown.

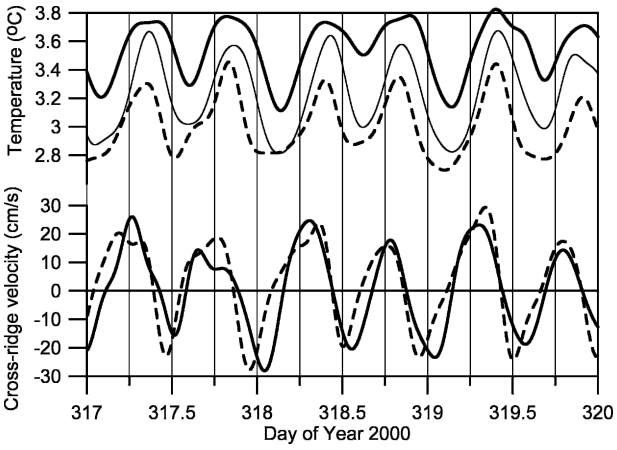

FIG. 3. (top) Low-pass-filtered temperature at 1165 (thick), 1295 (thin), and 1421 m (dashed), and (bottom) cross-ridge velocity at 1229 (solid) and 1373 m (dashed) over a 3-day period.

cates a fairly linear relationship with a slope of 0.06 psu $°C^{-1}$. There are small offsets between the T–S curves from the five sensors due to calibration error in T or C. The magnitude of these offsets is at most 0.004°C, if attributed solely to temperature error, or 0.0004 S m^{-1} if attributed solely to conductivity error. For purposes here we assume that θ and S are linearly related and that variations in θ are a reasonable proxy for density fluctuations over this narrow range of θ (2.5–4.0°C) and S (34.50–34.60).

3. Tidal flow: Basic description

The basic patterns of velocity and density variability at tidal frequency are examined using data low-pass filtered with a cutoff near 1/4 cph. The velocity is decomposed into cross-ridge (v, in the y direction, 35° clockwise of north) and along-ridge (u, in the x direction, 125° clockwise of north) components (Fig. 1). To demonstrate the tidal behavior, representative portions of the time series of v and T are shown in Fig. 3. The signal is dominated by the semidiurnal frequency with v and T at the same depth nearly 90° out of phase. Low-passed temperature decreases when the flow is upslope ($v < 0$), consistent with the upslope transport of colder water originating from deeper down the slope and temperature increases when the flow is downslope ($v > 0$). There is also significant variation with depth of the amplitude and phase of v and T, which is discussed below. An example of the unfiltered temperature time series for one day during spring tide is shown in Fig. 4.

a. Barotropic tide

The barotropic tidal model of Egbert (1997) provides a reference for the observed tidal motion. The model v component of the barotropic tidal velocity is shown in Fig. 5. Model velocity is dominated by the semidiurnal tides (M_2 and S_2); however, diurnal tidal components (K_1 and O_1) lead to a significant diurnal inequality. The strong spring–neap cycle is caused primarily by the M_2 and S_2 constituents, but the beating of K_1 and O_1 also contributes.

The observed low-passed v velocity at 1373 m is plotted for comparison with the barotropic prediction (Fig. 5). While there are significant differences, the observations show a similar pattern of the spring–neap cycle. Much of the difference between the model and observations is ascribed here to the presence of internal tides and waves.

A detailed comparison between the barotropic tide and the observations is shown in Fig. 6 for the four largest tidal constituents. The observed cross-ridge velocity amplitudes were estimated from a Fourier transform of a 59-day record, so that each tidal line is nearly centered on a harmonic. The frequency distribution of the observed amplitudes (Fig. 6a) generally follows that of the model barotropic tide. For example, the M_2 v velocity is the largest component, and the O_1 is the smallest in both model and observations. A comparison of the phase of the model barotropic tide and the observations indicates significant phase differences (Fig. 6b). In addition, the observations show a significant depth dependence in both amplitude and phase that is, of course, not present in the barotropic tide.

The cross-ridge component of the barotropic tide results in a significant vertical displacement with a maximum amplitude near the bottom. If the seafloor were

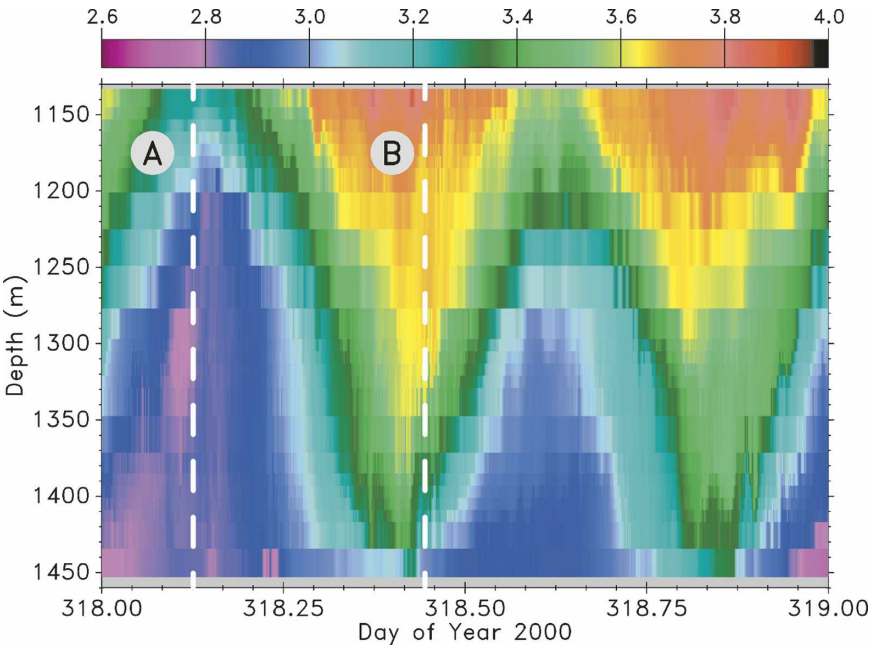

FIG. 4. Temperature for yearday 318. The data from each sensor are assumed to represent the temperature around the sensor. The two profiles A and B (dashed lines) are shown in Fig. 19.

level, there would be no vertical displacement at the bottom. However, for example, a cross-ridge M_2 barotropic tide at frequency ω with an amplitude of $v = 0.1$ m s^{-1} over a slope $s = 0.1$ results in a maximum vertical displacement of $2sv/\omega = 142$ m. In the barotropic model the amplitude of the vertical displacement decreases linearly with height above the bottom to match the surface elevation, which for this constituent is a negligible 0.13 m (Egbert 1997). The predicted displacement for the total barotropic tide (eight largest constituents) shows a strong spring–neap modulation and a marked diurnal inequality (Fig. 7). The observed displacement at 1325 m (Fig. 7), inferred from temperature using a mean vertical gradient, also shows a spring–neap cycle similar to the model barotropic tide. However, the observed displacement time series has a less pronounced diurnal inequality and thus would appear to have a greater ratio of semidiurnal to diurnal energy than does the model barotropic displacement.

The amplitude of the model vertical displacement of the tidal constituents can be compared with the observed displacement (Fig. 8). The barotropic predictions of M_2 and S_2 agree with the deepest and shallowest measurements. However, the observed amplitudes have a greater depth dependence than the barotropic predictions, reaching about 2 times the barotropic prediction at 100–150 m above the bottom. We suspect that most of the observed deviations from the barotropic model are due to the presence of the internal tide.

We have focused on the cross-ridge component of velocity, as it directly leads to internal tidal generation. The observed along-ridge rms velocity over a liberal semidiurnal frequency band (11–16-h period) is about 0.06 m s^{-1} as compared with the rms cross-ridge velocity of 0.10 m s^{-1} over the depth range 1200–1400 m. The inferred along-ridge horizontal tidal displacement scale is then about 500 m. Over these horizontal scales the variation in the along-ridge topography appears to be minimal, based on the high-resolution side-scan sonar (Fig. 1) (Eakins et al. 2003).

b. Kinematic description with baroclinic tides

To provide a framework for interpreting the observed overturning events, which are the central theme

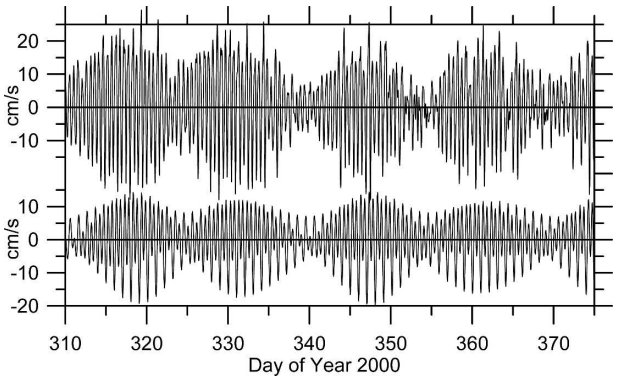

FIG. 5. (top) Low-pass-filtered cross-ridge velocity component measured at 1373 m, and (bottom) predicted barotropic cross-ridge tidal velocity from the model of Egbert (1997) using eight tidal constituents.

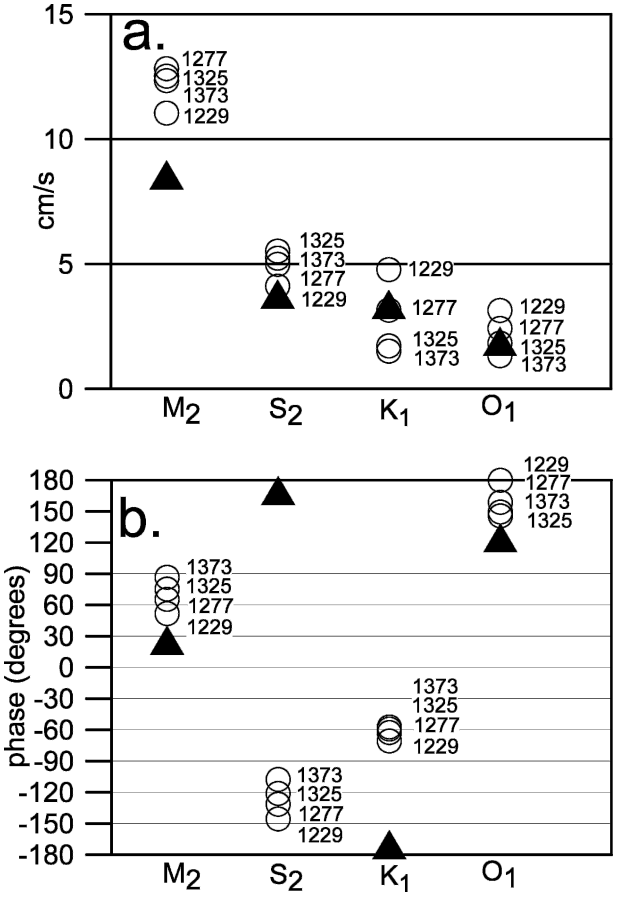

FIG. 6. (a) Amplitude and (b) phase of the cross-ridge velocity measured at four depths (1373, 1325, 1277, 1229 m) for four tidal constituents using a 59-day time series (circles). Predicted barotropic amplitude and phase of the cross-ridge velocity are calculated using the model of Egbert (1997) (triangles). Phase is referenced to the first data point in the data at 2232 UTC 3 Nov 2000.

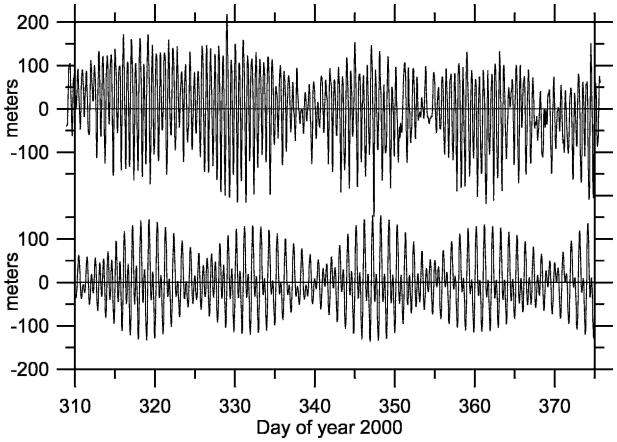

FIG. 7. (top) Vertical displacement inferred from low-pass-filtered temperature at 1325 m using a mean temperature gradient of 2.5×10^{-3} °C m^{-1}, and (bottom) predicted vertical displacement of barotropic tide at 1325 m from the model of Egbert (1997) using eight tidal constituents.

of this paper, a linear, kinematically self-consistent description of the observed tidal flow is presented. The kinematic description in two dimensions (y, z) is based on the low-pass-filtered velocity observed during spring tide, such as shown in Fig. 3. As a first-order description of the fluid flow, it is assumed that the observed frequency is purely M_2, even though the total tide is a sum of constituents. Missing from this description are nonlinearities in the velocity field that would appear as harmonics of the tide.

For guidance we appeal to some of the fundamental theoretical results of internal tide generation on sloping topography (e.g., Baines 1982; Rattray et al. 1969; Prinsenberg and Rattray 1975). Specifically, we consider the analytical results from Prinsenberg and Rattray (1975) showing internal wave generation over a continental slope in a constant-N ocean (their Fig. 5). In this model, internal waves are generated at the shelf break, from which high-amplitude beams of M_2 frequency appear to emanate at a slope α of the internal wave group velocity given by

$$\alpha = \left(\frac{N^2 - \omega_{M2}^2}{\omega_{M2}^2 - f^2} \right)^{1/2}$$

(e.g., Gill 1982, p. 259), where α is known as the critical slope. The water particles tend to oscillate back and forth along the lines of constant phase within the beam, and the phase propagates upward in the beam consistent with downward energy propagation from the topographic break.

The observed low-pass-filtered horizontal velocity also tends to show upward phase propagation (Fig. 3). Overall, many aspects of the geometry of the ridge (Fig. 2) are similar to the idealized Prinsenberg and Rattray (1975) case, where the mooring is located on a slope s that is very nearly equal to α. Since cross-ridge dependence was not measured, we assume for simplicity that the combined cross-ridge barotropic and internal tidal flow is everywhere parallel to the bottom vertically within a few hundred meters of the bottom. The vertical and horizontal velocity are then related by $w(z', t) = -sv(z', t)$, where z' is the coordinate normal to the bottom.

Using the low-passed observations during spring tide (Fig. 3), an idealization of the vertical structure of the amplitude and phase of the cross-ridge velocity v was made (Fig. 9). A free-slip boundary is assumed; no attempt has been made to include the frictional boundary layer because velocity data are lacking within 75 m of the bottom. The corresponding temperature field resulting from this oscillating flow is given by $T(z, t) = \Phi[z - \zeta(z, t)]$ (Fig. 10), where $\Phi(z)$ is the mean vertical

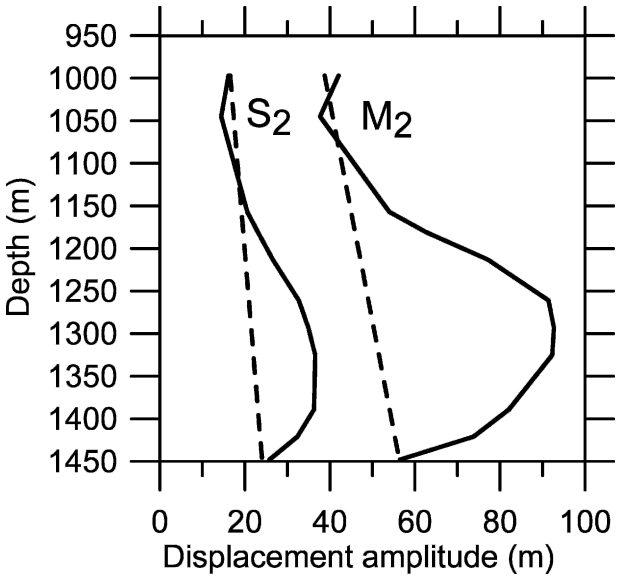

FIG. 8. Amplitude of vertical displacement as function of depth for M_2 and S_2 constituents inferred from temperature observations (solid line) and using the barotropic tidal model of Egbert (1997) (dashed line).

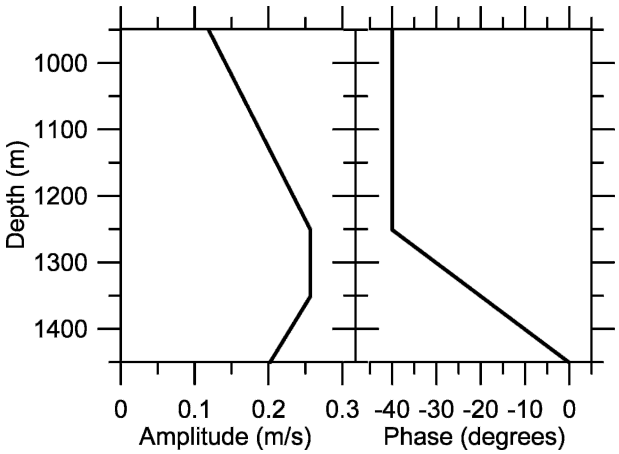

FIG. 9. Idealized amplitude and phase of cross-ridge velocity v as function of depth used in the kinematic model.

temperature profile and ζ is the vertical displacement defined by $[\partial\zeta(z, t)/\partial t] = w(z, t)$. This expression states that the temperature observed at time t and depth z is the temperature of the mean field that has been displaced to depth $z - \zeta(z, t)$ along a cross-ridge trajectory parallel to the bottom. Hence, although the velocity field is sinusoidal in time, the resulting isotherms are distorted sine waves. This is because the sheared cross-ridge velocity is parallel to the bottom and vertically advects the horizontally uniform mean temperature field. Since the velocity is always parallel to the bottom, the temporal pattern of isotherm displacement in Fig. 10 is the same along any cross-ridge line parallel to the bottom without a phase shift. The time sequence of the isotherms in (y, z) is shown in Fig. 11. This description is useful only locally in y near the mooring, as the constant topographic slope does not continue indefinitely. Note that the strength of the vertical temperature gradient varies over the tidal cycle because of the vertical divergence or strain. Most of the overturns occur in regions of weak gradient, as is explained in section 4.

4. Mixing

A striking feature of the temperature time series is the frequent occurrence of inversions in the vertical temperature profiles as measured by the moored sensor array. It is assumed below that an observed density inversion is the result of the rearrangement of the stable water column as a result of an instability. The timing and strength of these overturns are found to be highly correlated with the tidal forcing, and we make indirect estimates of the turbulent dissipation rate that would result from the collapse of these overturns.

a. Overturns

The measurement of a temperature inversion between a pair of sensors indicates the presence of an overturn. An objective method is implemented to quantify the size and strength of the overturn. We define the vertical extent of an overturn to be the turbulent patch height H. From the temperature sensor time series, H is defined to be the largest vertical separation between a pair of sensors in which the inversion is present (see the appendix). The sensors were spaced by multiples of 8 m vertically (except the deepest sensor) but with significant gaps. Hence, estimates of patch height are a lower bound; actual patch heights could be larger. Of course, any patch occurring entirely within a sensor gap will be missed altogether. A temperature inversion of greater than 0.004°C between sensors was required before an overturn was identified. We believe this is a conservative criterion, given the repeatability of the calibrations, the temperature adjustment procedure (section 2a), and the T–S correlation (section 2b).

The moored temperature data can be thought of as a profile every 2 min for a 2-month duration. By appealing to ergodicity, we assume at each depth that statistical quantities, such as mean values, can be estimated by temporal averaging.

There were 12 977 patches identified in the 47 520 total vertical profiles of θ. The cumulative distribution of patch height is given in Fig. 12. About one-fourth of the patches (3045) are the minimum resolvable 8 m. Regarding the depth dependence of the overturns, more patches are seen in the closely spaced sensor groups, where the more prevalent, smaller patches can

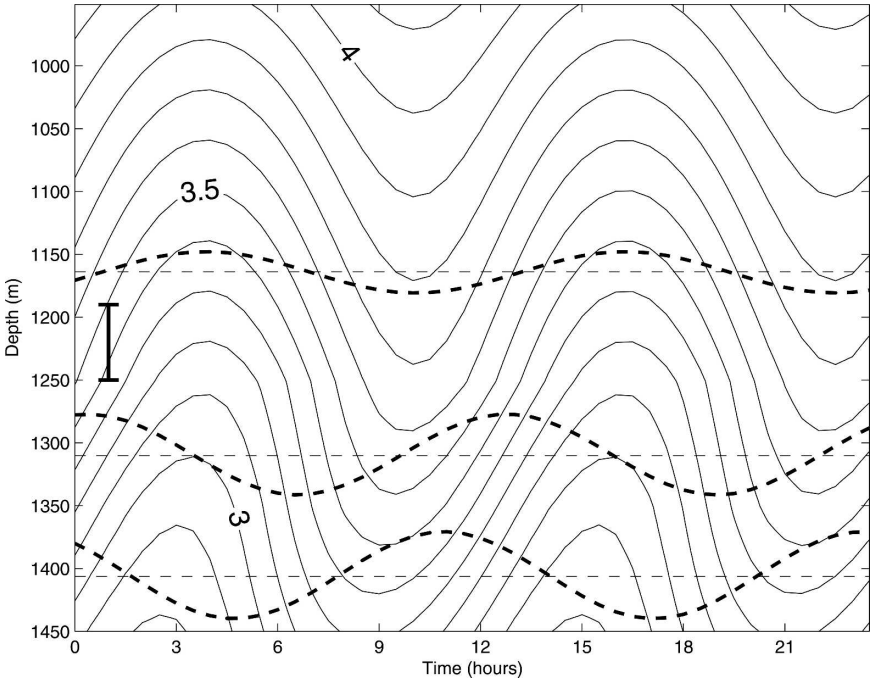

FIG. 10. Contour plot of temperature (°C) from kinematic model. Time series of N^2 are plotted on a linear scale at three depths (dashed lines). The mean of each series is $N^2 = 1$ cph^2, and the scale of the vertical bar is 1 cph^2.

be detected. Sensors that are more isolated see fewer overturns, as only the more rare, larger overturns can be detected. The fraction of the time that patches with height greater than 24 m occur at a given depth is shown in Fig. 13. While the sampling is uneven in the vertical direction, the probability of being within an overturn of significant size increases dramatically below 1300 m.

b. Thorpe scale L_T

If we assume that the observed density inversion is a signature of a breaking wave resulting from a shear or advective instability, then it may be useful to estimate the Thorpe scale L_T. The observed inverted density profile can be reordered to its assumed original state by moving the density observed at each depth to a new depth such that density increases monotonically with depth. The vertical distance that the density at each depth is moved is called the Thorpe displacement $d(z)$ (Dillon 1982). All of the points that are moved during reordering stay within the patch height H, as previously defined in section 4a (see appendix). The Thorpe scale L_T is the root-mean-square of $d(z)$ within the patch.

Calculation of L_T is somewhat problematic because of the limited number and irregular spacing of observations within a patch. The typical algorithm used to calculate Thorpe displacements and patch heights involves reordering the density points that have been interpolated onto a regular vertical grid. The points in the resultant reordered profile then also occur at the same regular vertical spacing. For these data an evenly spaced grid of $\Delta = 1$ m was chosen.

The Thorpe scale L_T estimated from the linearly interpolated profiles is plotted versus patch height H in Fig. 14. On average the trend is for larger patches to have larger L_T. The maximum possible Thorpe scale for a given H is an idealized "rotary" overturn, in which the water within the overturn is rotated 180° about the center of the patch, and is given by $L_T = \sqrt{1/3}H$ in the limit of Δ goes to 0 (Fig. 14). Another interesting calculation is to assume that during overturning the water parcels within a patch of height H are rearranged randomly and with equal probability. This results in an expected value of $L_T = \sqrt{1/6}H$, again in the limit Δ goes to 0 (Stansfield et al. 2001). However, the observed average L_T from the mooring data is about $0.5H$—a value between the expected value for the equal probability model and the maximum value for a given H.

Each of our individual estimates of a Thorpe scale is based on a smaller number of points than is typical for this type of analysis. However, the method of estimating a minimum overturn height H is robust (see the appendix). While there is not a deterministic relationship between H and L_T, they are clearly related. Linear interpolation maximizes the estimated Thorpe displace-

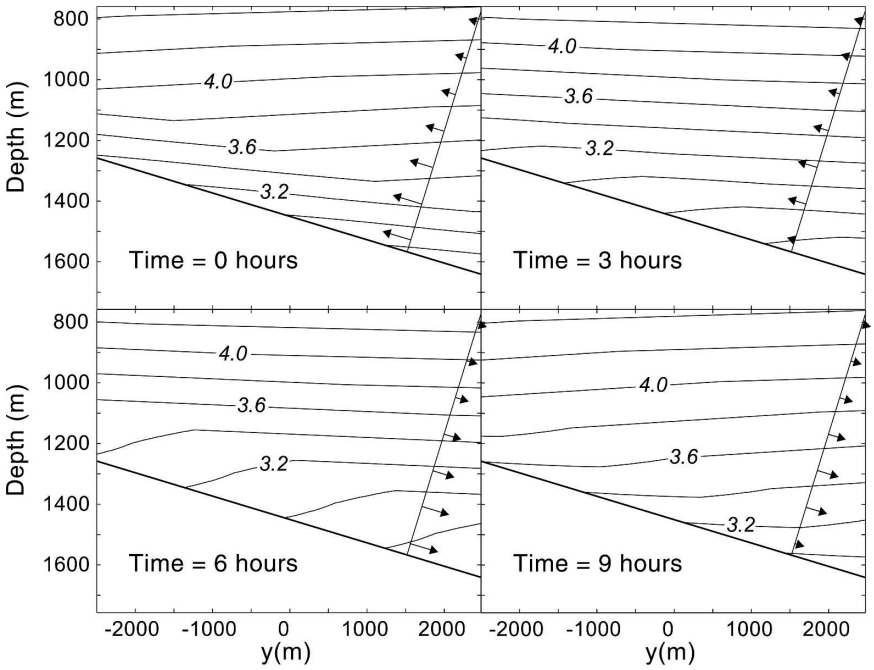

FIG. 11. Isotherms and velocity vectors of the kinematic model at four times during the semidiurnal cycle as a function of depth and cross-ridge distance. The mooring is located at $y = 0$.

ments within an overturn by effectively creating "rotary" overturns between depths where there are no data. If a different interpolation scheme were used, the resulting Thorpe scale would have been smaller. We explore the uncertainty introduced by this unresolved variability by considering the shape of the vertical wavenumber spectra of Thorpe displacement d. Note that the total variance of the Thorpe displacement spectrum is L_T^2. Microstructure measurements made within overturns show that the spectrum is proportional to $k^{-5/3}$ to k^{-2} with a maximum at $k = 1/L_T$ (Dillon and Park 1987; Wijesekera and Dillon 1997). The fact that the spectrum is red suggests that only the longer scales of d need to be resolved to estimate L_T because the contribution of the shorter-scale oscillations to the total variance is quite small. Hence, the coarse 8-m resolution and the relatively few points measured within a patch are not a severe limitation in estimating the Thorpe scale. This concept is explored further with a simple numerical experiment.

The numerical experiment consisted of randomly shuffling an initially linear profile of 20 points uniformly spanning the depth range H. The shuffle was performed 10^5 times, resulting in a distribution of L_T/H that is normally distributed with a mean of about $\sqrt{1/6}$. The spectrum of the Thorpe displacement was computed for each shuffle, and the realizations were sorted by spectral slope. On average the Thorpe scale is larger when spectra are redder because there are proportionately more large Thorpe displacements (Fig. 15). More specifically, when L_T/H lies between the maximum value possible ($\sqrt{1/3}$) for a rotary overturn and the average value for the random model ($\sqrt{1/6}$), the slope of the wavenumber spectrum of d is most consistent with the microstructure measurements. Since our estimates of L_T from observed H also fall between these limits, we infer that they are physically reasonable and that an increased vertical resolution would not have significantly changed the estimates of L_T. Variations of this experiment with different numbers of points and shuffles lead to the same fundamental results.

c. Stratification within an overturn

For all patch heights the square root of the average N^2 in the reordered overturns tends to be significantly lower than the average background buoyancy frequency $\overline{N}$ (Fig. 16). The values of $\overline{N}$, which vary from 1 to 1.2 cph over this depth range, are obtained from CTD observations several kilometers from the mooring site toward deeper water. However, virtually the same profile is obtained by using the average temperature from the moored sensors or the average historical CTD data from the area (Levitus and Boyer 1994). The predilection for the reordered gradient to be significantly lower than the background is addressed in section 4e. Note that at smaller patch heights estimates of N are

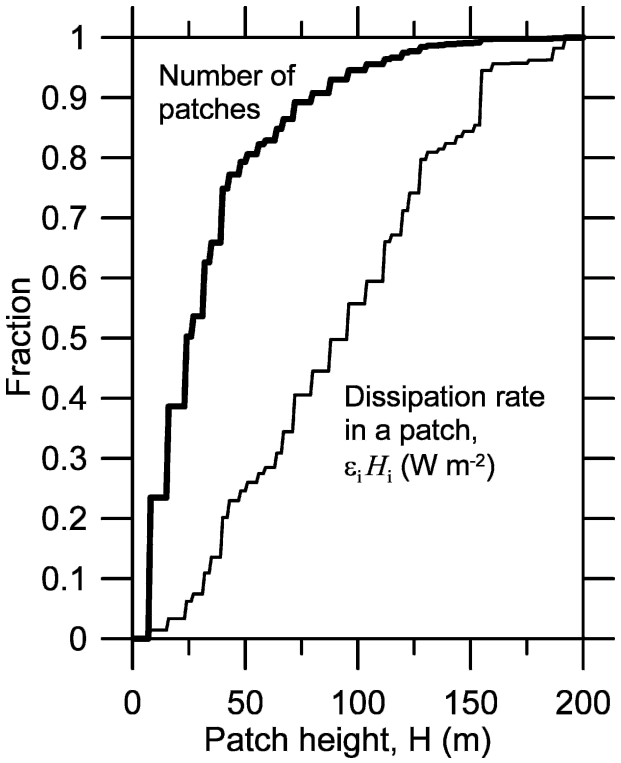

FIG. 12. Cumulative distribution of number of patches (solid line) and vertically integrated dissipation rate for each patch, $\varepsilon_i H_i$ (thin line), as function of patch height H. Total number of patches = 12 977.

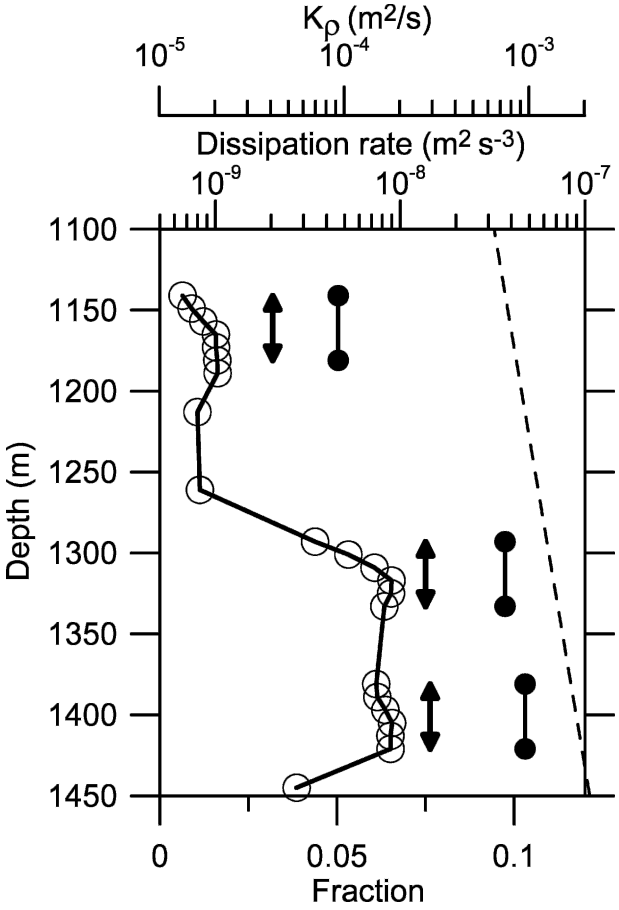

FIG. 13. The fraction of time at a given temperature sensor that there is an overturn of height greater than 24 m (circles). Also shown are three estimates of ε averaged over 40-m segments (arrows) and corresponding estimates of K_ρ (solid dots). The empirical function of K_ρ based on direct turbulence observations (Klymak et al. 2006) is also shown (dashed line).

biased toward higher values, since possible lower values of N have been eliminated by the imposed minimum criterion requiring a temperature difference greater than 0.004°C between sensors (section 4a).

d. Turbulent dissipation rate, ε

Physical reasoning and scaling arguments suggest that there may be a relationship between the Thorpe scale and the vertical scale of an overturn given by the Ozmidov scale, $L_O = (\varepsilon/N^3)^{1/2}$, where the appropriate N is estimated from the reordered profile, that is, the profile as assumed before overturning occurred (Thorpe 1977). Using independent observations of L_T and L_O, Dillon (1982) found $L_O/L_T = 0.8$ for a variety of oceanic conditions. The value of this ratio has been found in other studies to range from 0.64 to 0.95 (Itsweire 1984; Crawford 1986; Ferron et al. 1998). Recognizing that this ratio is not a universal constant and that it is not clear which value is the most appropriate here, we use $L_O/L_T = 0.8$ and estimate the dissipation rate in a patch as $\varepsilon = 0.64L_T^2N^3$ (m^2 s^{-3}). The vertically integrated dissipation rate over a single patch is then given by $\varepsilon_i H_i$ where H_i is the height of patch i with estimated dissipation rate of ε_i. The cumulative distribution of $\varepsilon_i H_i$ for all patches is given in Fig. 12 as a function of H. The contribution to the average energy dissipation is roughly the same for any H. While one-half of the dissipation is from patches greater than 80 m in height, these represent fewer than 5% of the total number of patches. Conversely, one-half of the patches are less than 24 m in height but contribute less than 5% of the energy dissipation. The overall time average of the dissipation rate of 2.6×10^{-3} W m^{-2} is obtained as a vertical integral over observations from 1150 to 1450 m. This is equivalent to a volume average ε of about 10^{-8} m^2 s^{-3}.

There is a strong depth dependence in ε essentially following the distribution of overturns (Fig. 13). Average ε is shown over three 40-m segments that each contain the same number of sensors separated by 8 m. The ε within 200 m of the bottom is about an order of

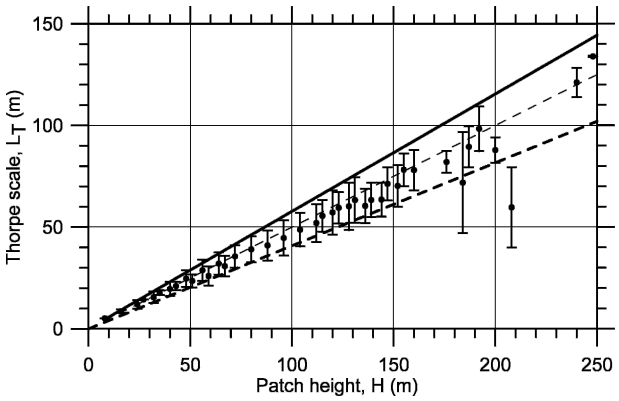

FIG. 14. Average observed Thorpe scale L_T for each patch height H; vertical bars indicate the standard deviation. Maximum possible L_T for given H is shown as solid line. Average L_T for given H for a random shuffle of the water column is shown as a heavy dashed line (Stansfield et al. 2001). The relationship $L_T/H = 0.5$ is shown by a thin dashed line.

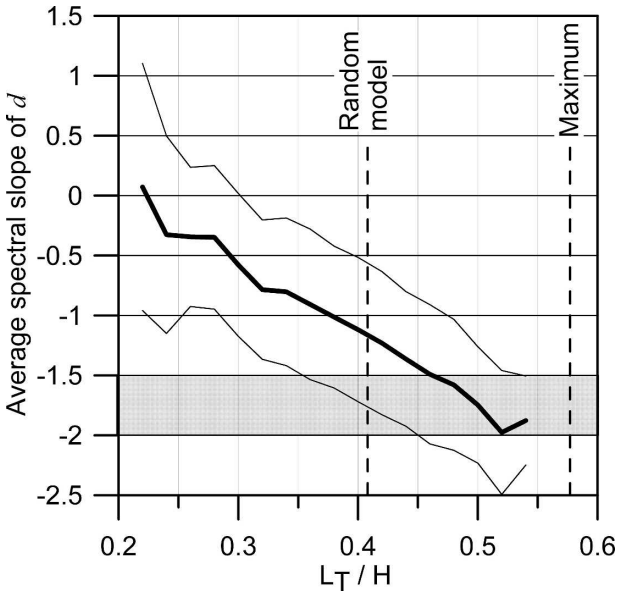

FIG. 15. Average (thick line) and standard deviation (thin line) of slope of Thorpe displacement spectra estimated from random shuffle model as function of Thorpe scale L_T. The realistic range of spectral slope is shaded based on the observations of Dillon and Park (1987) and Wijesekera and Dillon (1997).

magnitude higher than the observations 300 m from the bottom.

The diapycnal diffusivity is often estimated from ε by assuming the turbulent production equals dissipation model of Osborn (1980): $K_\rho = \Gamma\varepsilon/\overline{N}^2$, where the mixing efficiency Γ is usually taken to be 0.2 and $\overline{N}$ is the background average buoyancy frequency. Since $\overline{N}$ (1−1.2 cph) is nearly constant over this depth range, the depth profile of K_ρ varies like ε—ranging from 10^{-3} m^2 s^{-1} within 200 m of the bottom to 10^{-4} m^2 s^{-1} farther above. These values of K_ρ are well above the observed average value of 10^{-5} m^2 s^{-1} found in the deep ocean away from topography.

e. Correlation with the tide

To explore the temporal dependence of ε and its relation to the spring–neap tidal cycle, the time series of the vertically averaged ε (1141–1445 m) (Fig. 17) was smoothed with a running mean of 25 h to reduce diurnal and semidiurnal variability. The vertically averaged values of ε vary by more than an order of magnitude with a fortnightly period. For comparison, the predicted barotropic tidal amplitude (using eight tidal constituents) of the cross-ridge velocity is also shown in Fig. 17. The amplitude of the barotropic tide is clearly correlated with the estimated ε. The relative scaling of the ε and u axes is consistent with a power-law dependence of $\varepsilon \sim u^3$.

Besides the fortnightly modulation of mixing by the tide, there is a significant semidiurnal variation as well. This is demonstrated by estimating the number of patches and corresponding dissipation at a given depth as a function of an "effective tidal phase" (Fig. 18). Since the total tide is composed of constituents at several different frequencies, an effective phase is defined to vary linearly between the times of consecutive zero crossings of the model cross-ridge velocity using eight tidal constituents. If only one constituent were used, the time between zero crossings would be the same for each cycle. Since the time between zero crossings is dominated by the M_2 tide, the average time interval for a 2π change in effective phase is 12.42 h with a standard deviation of 1.32 h.

At the three depths shown in Fig. 18 there are two peaks in the number of overturns and dissipation over the tidal cycle. The larger of the peaks nearly coincides with the minimum in local N^2 or low-passed strain. The phase of this semidiurnal variation varies with depth, such that there is nearly a 180° phase shift between 1165 and 1405 m. As an illustration of this, compare the 1-day time series shown in Fig. 4 with the kinematic model in Fig. 10, where the phase has been adjusted qualitatively to match the start time of Fig. 4. Two profiles are shown from times separated by about one-half of a semidiurnal period (Fig. 19). Profile A is at a time when the upper part of the profile shows an increased vertical temperature gradient. The lower part of this profile shows a 187-m overturn with a Thorpe scale of 100 m and weak stratification in the reordered profile ($N = 0.32$ cph). This weak stratification could be due to a combination of internal wave straining and previous mixing of this water. A half tidal cycle later the profile B shows that the pattern has reversed. Now the in-

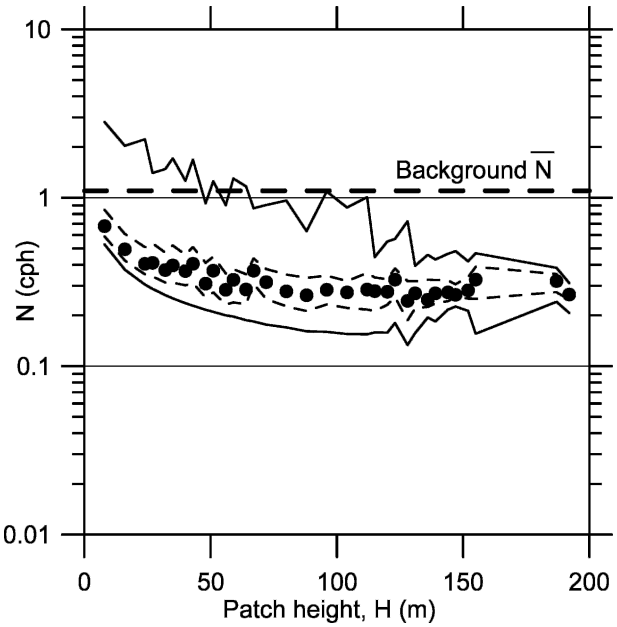

FIG. 16. Square root of average N^2 from reordered profiles for each patch as function of patch height (large dots). Background average N is also plotted. Note the bias toward larger values at small patch height (section 4c).

creased gradient is near the bottom, and the upper part of the profile has a large 128-m overturn. The reordered stratification in this overturn is extremely weak ($N = 0.19$ cph). This overturn also has a large Thorpe scale of 55 m, but because the stratification is so weak the estimate of $\varepsilon_i H_i$ is 1/15 that of profile A.

The smaller peaks in both number of overturns and dissipation over the cycle tend to occur roughly one-half of a semidiurnal period after the larger peaks (Fig. 18). The smaller peak is most pronounced at 1405 m, where it occurs near the time in the cycle when the stratification is strongest at that depth. An example of such an overturn occurring during the phase of the tide when the stratification is strong can be seen in profile B (Fig. 19) below the larger overturn in the weak stratification. Although this is a small overturn with patch height 8 m and $L_T = 5.1$ m, the dissipation ε is comparable to that in the large overturn above, since N is 5 times as large. However, since the patch height is much smaller, the contribution to the total vertically integrated dissipation is quite small.

Hence, it appears that overturns tend to occur at two phases of the semidiurnal tidal cycle. One phase at which overturns occur is when the strain of the internal tide weakens the stratification. The linear kinematic model shows how this straining can be created from a horizontally uniform density (temperature) field by the advection of a shear flow (Fig. 9) oscillating parallel to the slope (Fig. 10). This oscillating shear is presumably the internal tide generated from the interaction of the barotropic tide with the local topographic slope (e.g., Prinsenberg and Rattray 1975). The correlation of the number of overturns and dissipation with the inverse of the local N^2 occurs at all depths: more overturns occur when the background stratification is weaker.

The other phase of the tide at which overturns occur is when the low-passed N^2 is the highest. This situation is apparently similar to the one found by Aucan et al. (2006) where the overturns occur mostly within 100 m or so of the bottom boundary and are often accompa-

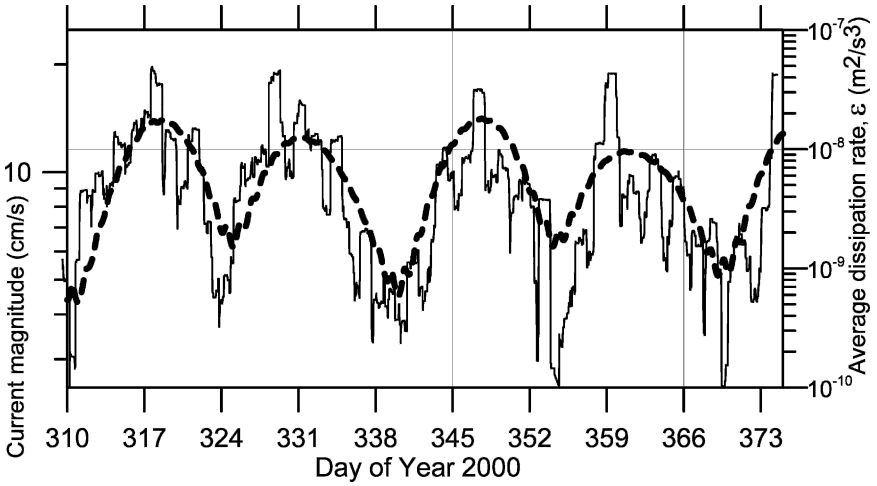

FIG. 17. Magnitude of cross-ridge tidal velocity (dashed) and estimated ε (solid) plotted as a function of time. The ε series is the vertical average from 1141 to 1445 m; tidal velocity is from the model of Egbert (1997) using eight tidal constituents. Both time series are smoothed with a 25-h running mean. The log scales are set such that 1 decade in velocity is equal in length to 3 decades in ε, consistent with $\varepsilon \sim u^3$.

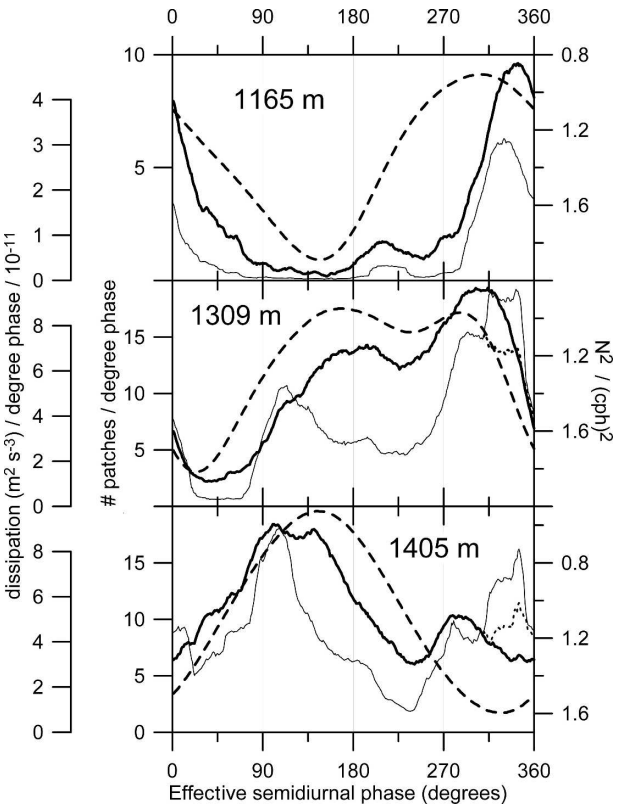

FIG. 18. The number of patches (solid thick line) and dissipation (sold thin line) observed at three depths plotted as a function of tidal phase. Effective tidal phase is defined to range from 0° to 360° between successive zero crossings of the cross-ridge barotropic tide velocity from the model of Egbert (1997) using eight tidal constituents. Also plotted is N^2 calculated from the low-pass filtered temperature gradient around the depth of interest (dashed line); note axis increases downward. The dissipation with the removal of the 6 largest overturns is also shown (dotted line). All series are averaged with a running mean spanning 37° of phase.

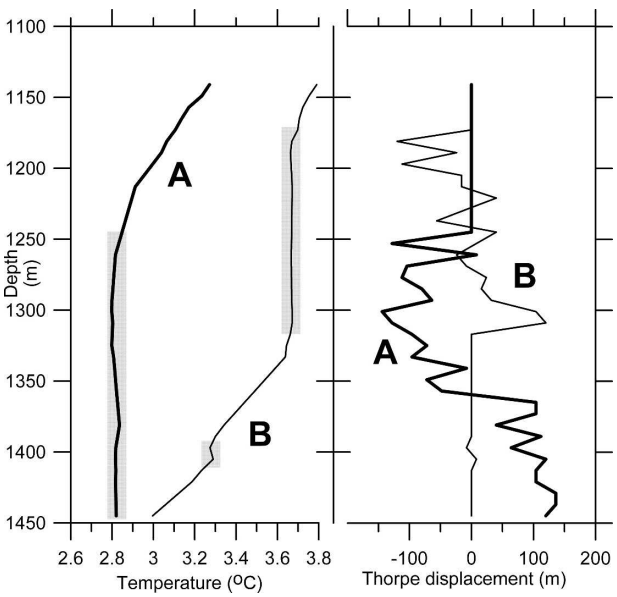

FIG. 19. (left) Vertical profiles A (thick line) and B (thin line) at the times of the dashed lines in Fig. 4. The depth ranges of overturns are indicated by shading. (right) The corresponding Thorpe displacements.

nied by strong jumps in density and high-frequency oscillations of significant amplitude (see examples in Fig. 4 at days 318.375 and 318.875). While there are fewer overturns during this phase of the tide, the overturns of this highly stratified water tend to have higher dissipation. This can be demonstrated qualitatively by recalculating the phase-dependent dissipation after removing only the six most energetic overturns (Fig. 18). The resulting dissipation indicates a significantly lower peak in dissipation at high N.

The simple linear kinematic model presented here provides a self-consistent first-order description of the velocity and temperature fields in depth and time. One significant shortcoming is that nonlinearity is, undoubtedly, important in the growth of the tidal oscillations that eventually lead to overturns. Tidal variations in vertical shear and N in the kinematic model result in minima of Richardson number at two phases per tidal cycle. The phase of low Richardson number did not correlate well with the periods of more frequent overturns. This could be due in part to phase changes related to the nonlinearity. Furthermore, Richardson number evaluated at this scale may not be the most relevant parameter to characterize the instability.

5. Comparison with other observations

The observations during HOME Survey clearly show evidence of enhanced mixing near steep topography and an association of that mixing with the tide. Finnigan et al. (2002) describe overturns and ε estimated from Thorpe scales on the ridge near the mooring site using CTD casts at station 6 of the Hawaiian Ocean Time-Series (HOT) program (Karl and Lukas 1996). Their average profile of ε in water depth of 2500 m showed a near-bottom increase of about an order of magnitude over mid-depth. The depth dependence of the HOT CTD data is similar to the result presented here for 1450-m water depth, where the estimated dissipation within 200 m of the bottom is about an order of magnitude greater than that estimated from depths shallower than 1250 m (Fig. 13).

An analysis of the direct observations of turbulence made by many investigators during HOME showed a significant increase in dissipation as the bottom is approached, resulting in an increase in K_ρ of about a factor of 10 above the values obtained at mid-depths (Klymak et al. 2006). They summarize the results from

many direct turbulence measurements by constructing an empirical estimate of average K_ρ as a function of depth and cross-ridge position. This function is plotted along with our estimated profile of K_ρ in Fig. 13. The values near the bottom are very close to this function; however, our estimates of K_ρ decrease more rapidly with height above the bottom. Unlike the moored observations, the few time series of turbulence measurements did not show as strong a spring–neap cycle, as ε varied only by a factor of 2 (Klymak et al. 2006). The strong tidal modulation may be a feature of near-bottom observations that was missed in the turbulence sampling.

Evidence of tidally driven turbulence in the deep ocean has previously been observed in the Atlantic Ocean. Observations by Polzin et al. (1997) in the Brazil Basin indicate increased diffusivity K_ρ of up to 5×10^{-4} m^2 s^{-1} above the rough topography of the Mid-Atlantic Ridge, while background levels of order 10^{-5} m^2 s^{-1} were seen over the smoother abyssal plain. Comparisons between the variation of total ε and the speed of tidal currents (St. Laurent et al. 2001, their Fig. 4; Ledwell et al. 2000) indicate a correlation with the spring–neap cycle similar to that shown in Fig. 17.

Other deep-water tidal observations over a slope near the Hebrides (1705-m water depth) have been reported by Thorpe et al. (1990). The local slope is 4° and is close to critical for the semidiurnal internal tide, similar to the Big Boy site. The observations within the bottom 200 m of the water column show significant semidiurnal tidal oscillations with a pronounced temporal asymmetry, such that at a fixed depth the temperature cools more rapidly than it warms. The phase shift with depth is such that the phase appears to propagate downward. This implies an upward energy propagation that is opposite the sense of the HOME Big Boy observations. However, in both the Hebrides and HOME data, overturns occur most often when the gradient is weakest. Also, the asymmetry in the temperature signal at the Hebrides site is more pronounced than at HOME, with much of the temperature transition from warm to cold water occurring over a relatively short 1–2-h period. Thorpe (1992) interprets the Hebrides data as the result of a spatial nonlinearity that develops into a "thermal front" as the wave propagates up the slope, similar to what might develop from wave reflection (Slinn and Riley 1998). In the kinematic description of the HOME data we envision the displacement by the cross-ridge oscillations to be essentially in-phase parallel to the bottom—as a beam of internal waves propagating nearly parallel to the bottom (Fig. 11). Of course, there could be some phase change parallel to the bottom, which could have been determined only by having multiple moorings across the slope.

Measurements of tidal variability in very deep water at Porcupine Bank (3447-m water depth) over the continental slope southwest of Ireland have also been reported by Thorpe (1987). The Porcupine Bank tidal signal is similar to that of the Hebrides with significant temporal asymmetry and a downward phase velocity. Temperature inversions at Porcupine Bank were observed to occur most frequently when the stratification was the weakest, similar to the pattern observed at both the Hebrides and the HOME sites.

Tidal currents interacting with seamounts and shelf breaks in shallower water (100–200 m) have been found to generate significant turbulence away from the topography. Regions of internal tidal energy radiating along beams from the flanks of Cobb Seamount (Lueck and Mudge 1997) and from the continental shelf break (Lien and Gregg 2001) have been found to be sites of enhanced dissipation. The present observations of high dissipation may also be within an internal tidal beam. However, in contrast to these examples where the beam becomes increasingly far from the bottom as the beam leaves the generation site, the HOME tidal beam roughly follows the topography around the mooring site.

Observations above the flanks of Fieberling Guyot, an isolated topographic feature in the North Pacific Ocean, provide an interesting comparison with these results. Moored and profiling measurements were made over Fieberling Guyot in water depth of 1500 m, comparable to that of the Big Boy site (Toole et al. 1997; Eriksen 1998). Although N at both sites is about 1 cph at that depth, Fieberling has a much steeper slope (0.45) than the HOME Big Boy site, resulting in a critical frequency (0.42 cph) that is much higher than the semidiurnal tide. Fine structure and turbulence at Fieberling are enhanced near the bottom. Profiling data show that about 5% of the water column is unstable within 500 m of the bottom compared to no density inversions at shallower depths (Toole et al. 1997). Moored temperature measurements from a yearlong deployment of sensors separated by 10 m indicate that temperature inversions exist about 10% of the time in the bottom 60 m (Eriksen 1998). The overturns observed at HOME are also concentrated near the bottom; overturns greater than 24 m are present about 10% of the time at any depth in the bottom 200 m (Fig. 13). Direct turbulence measurements above the Guyot flank yield an ε of $(4.1 \pm 1.5) \times 10^{-9}$ m^2 s^{-3} within 100 m of the bottom. This is about an order of magnitude higher than the ε observed at the same depth in the far field of the Guyot. The observed increase in finescale

shear, strain, and turbulence near the Guyot is thought to be due, at least in part, to reflection of internal waves off the bottom. Although determining the specific processes responsible for the dissipation is difficult, it is clear that enhanced dissipation and mixing extends hundreds of meters above the bottom. As with the HOME observations, the region of increased turbulence near the bottom extends beyond the height of a typical frictional boundary layer. Internal waves seem to be involved in creating a thick effective boundary layer in both cases. However, Fieberling and HOME differ on the suspected source of the internal wave energy. The Fieberling study suggests that the energy source is the background internal wave field that is modified by reflection off topography, while at HOME it appears that tidal forcing generates a local nonlinear internal response leading to instability and overturning.

Observations of vertical overturns in the upper ocean (100–400 m) and far from topography in 1500-m water depth off California provide another interesting comparison with the observations at HOME (Alford and Pinkel 2000). A similar relationship between the strain and the existence of overturns is found despite very different forcing and environmental conditions. Using the reordered density profile to represent the stratification before overturning occurred, Alford and Pinkel (2000) observed that the overturns occurred preferentially at times where preexisting stratification was weak (low N). The cumulative distribution function of ε versus reordered N^2 shows that 80% of the ε occurred when $N^2 < 1/2\overline{N}^2$ (Fig. 20). The analogous distribution function for HOME is remarkably similar. However, a significant distinction between the datasets is that the reordered N^2 from within HOME overturns is not representative of the stratification surrounding the overturns. At HOME the stratification (N^2) above and below an overturn is usually higher than the background mean, whereas Alford and Pinkel (2000) find that the region around the overturn also has relatively weak stratification when compared with the background mean. Stated another way, in the Alford and Pinkel (2000) data there is usually a scale separation between the vertical scales of the strain field and the overturns themselves. This difference relative to HOME may be due to differences of the scales of the internal wave field that are responsible for creating the vertical straining.

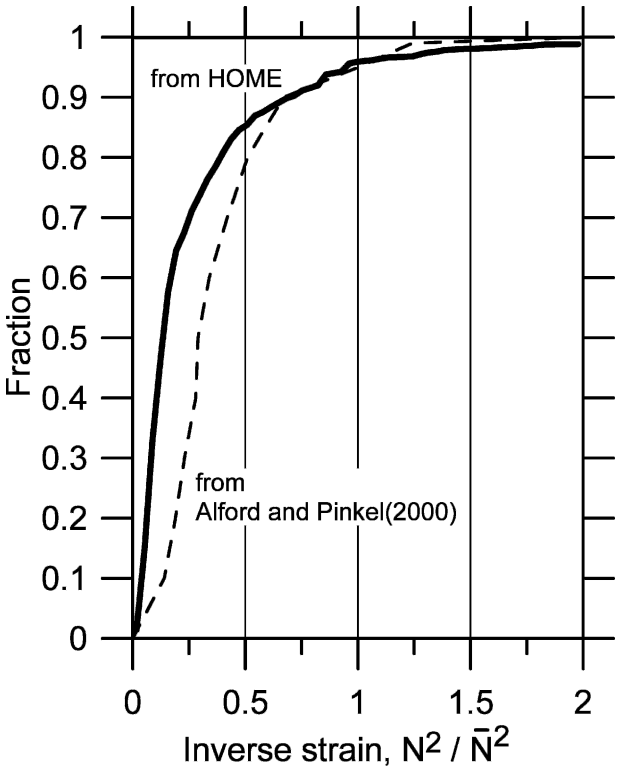

FIG. 20. Cumulative distribution of ε as function of inverse strain $N^2/\overline{N}^2$ (thick line). Also plotted is the distribution from the northeast Pacific Ocean given by Alford and Pinkel (2000) (dashed line).

6. Summary and conclusions

Overturns greater than 24 m high were often observed in the time series measured on the flanks of the ridge extending northwest from Oahu, Hawaii, during the HOME Survey project. The mooring was located in a water depth of 1453 m on a slope of about 0.08 (4.5°), which is nearly the slope of the internal wave group velocity at semidiurnal frequency (Fig. 1). The mooring was designed to sample the lower 500 m of the water column for indirect evidence of tidally induced mixing (Fig. 2).

The M_2 barotropic tidal current ellipse is oriented in the cross-ridge direction (Egbert 1997), favorable for generation of a large-amplitude internal tidal response. The cross-ridge velocity and temperature time series are dominated by significant tidal oscillations. While M_2 is the dominant tidal constituent, the displacement amplitude of S_2 is about 1/2 of the amplitude of M_2, which contributes to a significant spring–neap variation (Fig. 6). The diurnal tide, primarily K_1 and O_1, is also significant and leads to a diurnal inequality. The observed tidal oscillation, including both barotropic and internal tide, is described with a simple kinematic model such that flow is everywhere parallel to the cross-ridge bottom slope (Figs. 8 and 9). The velocity amplitude and phase of this tidal flow vary with distance from the bottom, creating significant vertical shear (Figs. 3 and 8). This shear strains the density field

and leads to tidal oscillations in the vertical density gradient (Fig. 9). The phase structure in the 200 m above the bottom is consistent with upward phase propagation. This implies energy propagation downslope from a source farther up on the ridge, such as the break in slope at 1100 m (Fig. 2). This picture of the phase is consistent with the analytical internal tide model of Prinsenberg and Rattray (1975) for a slope slightly steeper than the critical angle. Our kinematic description neglects any phase change in the direction parallel to the cross-ridge slope, at least in the region around the mooring site. This view differs from the interpretation of moored results from the Hebrides slope, where a strong along-slope gradient is assumed that leads to formation of a thermal front (Thorpe 1992).

Density overturns are inferred from temperature profiles measured by the mooring every 2 min for 2 months. Patch height and Thorpe scales were estimated for each overturn (see the appendix). As a check on the methodology, the relationship between the estimates of L_T and H was explored and found to be consistent with physically reasonable expectations of the Thorpe displacement.

Estimates of ε were made by associating the Thorpe scale with the Ozmidov scale (Fig. 12). Overall, the number and strength of the overturns are greatest in the 200 m near the bottom (Fig. 13). Above 1250 m, overturns are less frequent. The average ε between 1300 and 1450 m for the entire experiment is about 10^{-8} $m^2 s^{-3}$, corresponding to an average K_ρ of 10^{-3} $m^2 s^{-1}$ (Fig. 13). These values are consistent with an empirical function based on direct turbulence measurements made during HOME (Klymak et al. 2006). Our measurements indicate that near-bottom values of both ε and K_ρ decrease by about an order of magnitude by 1200-m depth. Although the measured values of K_ρ are significantly higher than the typical deep-open ocean values, an extrapolation assessing the overall dissipation created by the entire Hawaiian Ridge system suggests that the elevated diffusivity is not enough to make up the difference between the 10^{-4} $m^2 s^{-1}$ predicted by Munk (1966) and the observed 10^{-5} $m^2 s^{-1}$ in the deep open ocean (Klymak et al. 2006).

Observed overturns are also highly correlated with the tide. The spring–neap variation in the cross-ridge velocity is strongly correlated with the frequency of overturns and estimates of dissipation rates. The 24-h running average shows a variation in ε by at least an order of magnitude (Fig. 17). There is also correlation over the phase of the semidiurnal tide itself. The overturns occur primarily during the 3–4 h when the vertical strain is greatest (Fig. 18). At times, overturns also occur within 200 m of the bottom when the internal tidal strain has created relatively high stratification. These events are less regular and usually accompanied by high-frequency oscillations of order 1 h. Overturns observed in a similar environment during this phase of the tide were initially reported by Aucan et al. (2006).

Since the stratified fluid is being forced near its resonant frequency, a nonlinear response is anticipated, and the potential for generating turbulence seems likely. Viewed another way, the semidiurnal internal response is nearly trapped to the slope and cannot easily propagate away as free internal waves. Bottom friction may also play a role in the evolution of the flow. A dynamical analysis of the energy pathway from the barotropic tide to the generation of overturns is left for future study, but it is apparent from the observations of overturns that the generation of inversions is correlated with both the phase and amplitude of the tidal oscillations.

On average, the reordered N within the overturns is lower by a factor of 0.3–0.4 of the background $\overline{N}$. This is consistent with the kinematic description, in which the internal tidal response first strains the mean density field, leading to a region of low N that subsequently overturns. Hence, the observed low-N regions are probably due to both reversible vertical straining and the irreversible mixing within overturns. Continued tidal forcing might then tend to continue the overturning process, leading to a larger overturn, which continues to mix the water even more. This would be analogous to a spilling breaker, where the forcing maintains a breaking state. However, as far as we can tell, each cycle appears to begin again with stratified water. This suggests that mixed water is being flushed or advected away from the ridge and that the turbulence is not merely mixing already mixed water. The process by which the mixed water escapes the slope is important and is not easily assessed from these direct measurements. Further progress is likely through use of a dynamical numerical model to help to interpret these observations.

Acknowledgments. We gratefully acknowledge Rob Pinkel in organizing HOME and appreciate the valuable discussions with the many PIs involved. We thank Walt Waldorf for his skill in leading the mooring program. The successful deployment from the R/V *Wecoma* was due to the efforts of Captain Danny Arnsdorf, Marine Technician Marc Willis, and the entire crew. We thank the entire crew on the NOAA ship R/V *Ka'Imimoana* for the successful recovery. The data processing and organization were due to the efforts of Steve Gard. We appreciate the support of the National Science Foundation through Grants OCE-9819523 and

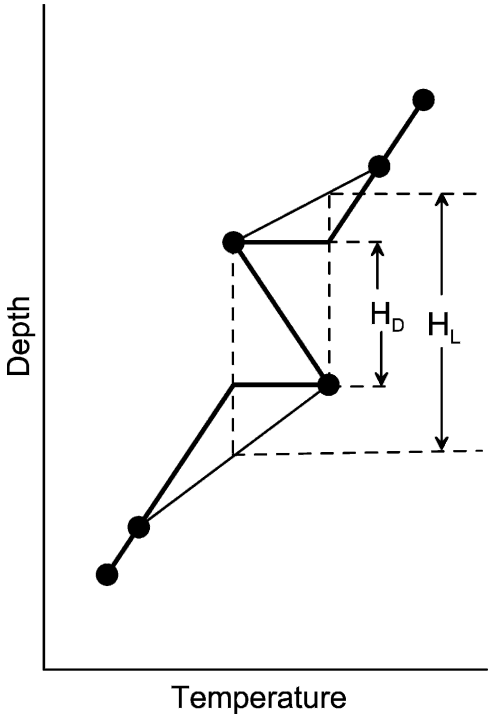

FIG. A1. A linear temperature profile after the occurrence of a "rotary" overturn of patch height H_D (thick line). Instrument depths are shown as dots. If the temperature profile is linearly interpolated (thin line) before reordering, then a patch height of H_L is estimated.

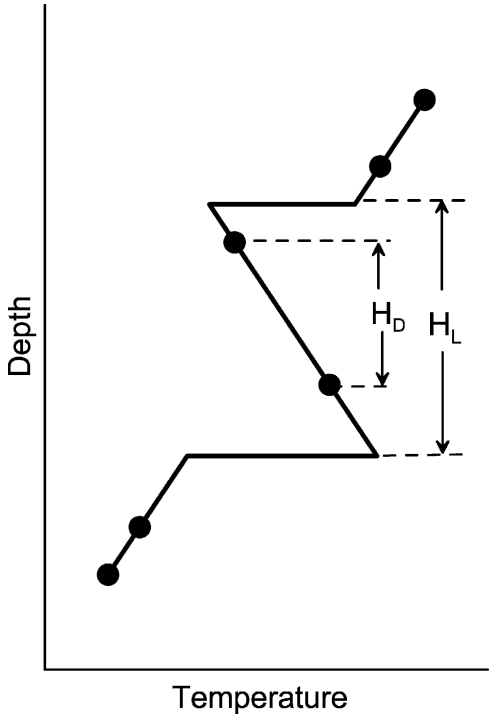

FIG. A2. A linear temperature profile after the occurrence of a "rotary" overturn of height H_L (thick line). If the temperature profile is reordered using only temperature measured at the instrument depths (dots), then a minimum estimate of the patch height H_D is calculated.

-9819532, and the efforts of program manager Eric Itsweire in overseeing the HOME project. This paper was greatly improved by the careful reading and insightful comments of two anonymous reviewers.

APPENDIX

Estimating Patch Height and Thorpe Scale from Unevenly Spaced Observations

a. Patch height

We have adopted a conservative estimator for patch height H. By using only temperatures measured at the sensor depths, the estimate of H is a minimum. For example, consider an initially linear temperature profile that has been altered by a perfect rotary overturn (Fig. A1, thick line). Assume observations are made only at the unevenly spaced sensors indicated by the dots. Reordering this observed temperature profile, such that temperature decreases with depth, requires that only the temperatures observed at two of the depths are exchanged. The patch height H_D (where the subscript D stands for discrete sensors) is then given by the depth difference. This patch height estimate H_D is consistent with the assumption of an overturn of the linear temperature profile. In this case, the full vertical extent of the overturn has been captured by the discrete observations. If, instead, we suppose the temperature between the discrete sensor depths were first linearly interpolated (Fig. A1, thin line), then an overestimate (H_L) of the actual rotary overturn would result when the profile is reordered.

To see that H_D is a minimum estimate, consider another overturn of the same initial linear profile (Fig. A2, thick line) observed with the same sensor array. It is clear, in this case, that the estimate based on discrete sensors (H_D) is an underestimate of the actual overturn scale H_L.

This method and reasoning can be extended to larger and more complicated profiles. In practice, there may be a series of smaller inversions within larger inversions. When this occurs the largest inversion is taken to be H_D.

b. Thorpe scaling

Once the top and bottom boundaries of the minimum patch height H_D have been determined, temperature values are estimated at 1-m vertical spacing by linear interpolation. This uniformly spaced profile is then reordered, and the Thorpe displacement and scale are estimated in the usual way. The consequences

of using linear interpolation within the patch are explored in section 4b. The important point is that to ensure a minimum estimate of the Thorpe scale the reordering is restricted to be within the minimum patch height H_D.

REFERENCES

Alford, M. H., and R. Pinkel, 2000: Observations of overturning in the thermocline: The context of ocean mixing. *J. Phys. Oceanogr.,* **30,** 805–832.

Armi, L., 1978: Some evidence for boundary mixing in the deep ocean. *J. Geophys. Res.,* **83,** 1971–1979.

Aucan, J., M. A. Merrifield, D. S. Luther, and P. Flament, 2006: Tidal mixing events on the deep flanks of Kaena Ridge, Hawaii. *J. Phys. Oceanogr.,* **36,** 1202–1219.

Baines, P. G., 1982: On internal tide generation models. *Deep-Sea Res.,* **29,** 307–338.

Boyd, T., M. D. Levine, S. R. Gard, and W. Waldorf, 2002: Mooring observations from the Hawaiian Ridge: November 2000–January 2001. Data Rep. 185, COAS Ref. 2002-1, College of Oceanic and Atmospheric Sciences, Oregon State University, Corvallis, OR.

Crawford, W. R., 1986: A comparison of length scales and decay times of turbulence in stably stratified flows. *J. Phys. Oceanogr.,* **16,** 1847–1854.

Dillon, T. M., 1982: Vertical overturns: A comparison of Thorpe and Ozmidov scales. *J. Geophys. Res.,* **87,** 9601–9613.

——, and M. M. Park, 1987: The available potential energy of overturns as an indicator of mixing in the seasonal thermocline. *J. Geophys. Res.,* **92,** 5345–5353.

Eakins, B. W., J. E. Robinson, T. Kanamatsu, J. Naka, J. R. Smith, E. Takahashi, and D. A. Clague, 2003: *Hawaii's Volcanoes Revealed.* Geologic Investigation Series I-2809, USGS.

Egbert, G. D., 1997: Tidal data inversion: Interpolation and inference. *Progress in Oceanography,* Vol. 40, Pergamon, 53–80.

——, and R. D. Ray, 2000: Significant dissipation of tidal energy in the deep ocean inferred from satellite altimeter data. *Nature,* **405,** 775–778.

——, and ——, 2001: Estimates of M2 tidal energy dissipation from TOPEX/Poseidon altimeter data. *J. Geophys. Res.,* **106,** 22 475–22 502.

Eriksen, C. C., 1998: Internal wave reflection and mixing at Fieberling Guyot. *J. Geophys. Res.,* **103,** 2977–2994.

Ferron, B., H. Mercier, K. Speer, A. Gargett, and K. Polzin, 1998: Mixing in the Romanche Fracture Zone. *J. Phys. Oceanogr.,* **28,** 1929–1945.

Finnigan, T. D., D. S. Luther, and R. Lukas, 2002: Observations of enhanced diapycnal mixing near the Hawaiian Ridge. *J. Phys. Oceanogr.,* **32,** 2988–3002.

Gill, A. E., 1982: *Atmosphere–Ocean Dynamics.* Academic Press, 662 pp.

Gregg, M. C., 1989: Scaling turbulent dissipation in the thermocline. *J. Geophys. Res.,* **94,** 9686–9698.

Itsweire, E. C., 1984: Measurements of vertical overturns in a stably stratified turbulent flow. *Phys. Fluids,* **27,** 764–766.

Karl, D. M., and R. Lukas, 1996: The Hawaii Ocean Time Series (HOT) program—Background, rationale and field implementation. *Deep-Sea Res.,* **43B,** 129–156.

Klymak, J. M., and Coauthors, 2006: An estimate of tidal energy lost to turbulence at the Hawaiian Ridge. *J. Phys. Oceanogr.,* **36,** 1148–1164.

Ledwell, J. R., A. J. Watson, and C. S. Law, 1993: Evidence for slow mixing across the pycnocline from an open ocean tracer release experiment. *Science,* **364,** 701–703.

——, E. T. Montgomery, K. L. Polzin, L. C. St. Laurent, R. W. Schmitt, and J. M. Toole, 2000: Evidence for enhanced mixing over rough topography in the abyssal ocean. *Nature,* **403,** 179–182.

Levitus, S., and T. Boyer, 1994: *Temperature*. Vol. 4, *World Ocean Atlas 1994,* NOAA Atlas NESDIS 4, 117 pp.

Lien, R.-C., and M. C. Gregg, 2001: Observations of turbulence in a tidal basin and across a coastal ridge. *J. Geophys. Res.,* **106,** 4575–4591.

Lueck, R. G., and T. D. Mudge, 1997: Topographically induced mixing around a shallow seamount. *Science,* **276,** 1831–1833.

Merrifield, M. A., and P. E. Holloway, 2002: Model estimates of M2 internal tide energetics at the Hawaiian Ridge. *J. Geophys. Res.,* **107,** 3179, doi:10.1029/2001JC000996.

Munk, W. H., 1966: Abyssal recipes. *Deep-Sea Res.,* **13,** 707–730.

——, and C. Wunsch, 1998: Abyssal recipes II: Energetics of tidal and wind mixing. *Deep-Sea Res.,* **45,** 1977–2010.

Osborn, T. R., 1980: Estimates of local rate of vertical diffusion from dissipation measurements. *J. Phys. Oceanogr.,* **10,** 83–89.

Pinkel, R., and Coauthors, 2000: Ocean mixing studied near Hawaiian Ridge. *Eos, Trans. Amer. Geophys. Union,* **81,** 545, 553.

Polzin, K. L., J. M. Toole, J. R. Ledwell, and R. W. Schmitt, 1997: Spatial variability of turbulent mixing in the abyssal ocean. *Science,* **276,** 93–96.

Prinsenberg, S. J., and M. Rattray Jr., 1975: Effects of continental slope and variable Brunt–Vaisala frequency on the coastal generation of internal tides. *Deep-Sea Res.,* **22,** 251–263.

Rattray, M., Jr., J. G. Dworski, and P. E. Kovala, 1969: Generation of long internal waves at the continental slope. *Deep-Sea Res.,* **16,** 179–195.

Rudnick, D. L., and Coauthors, 2003: From tides to mixing along the Hawaiian Ridge. *Science,* **301,** 355–357.

Slinn, D. N., and J. J. Riley, 1998: Turbulent dynamics of a critically reflecting internal gravity wave. *Theor. Comput. Fluid Dyn.,* **11,** 281–303.

Stansfield, K., C. Garrett, and R. Dewey, 2001: The probability distribution of the Thrope displacement within overturns in Juan de Fuca Strait. *J. Phys. Oceanogr.,* **31,** 3421–3434.

St. Laurent, L. C., J. M. Toole, and R. W. Schmitt, 2001: Buoyancy forcing by turbulence above rough topography in the abyssal Brazil Basin. *J. Phys. Oceanogr.,* **31,** 3476–3495.

Thorpe, S. A., 1977: Turbulence and mixing in a Scottish loch. *Philos. Trans. Roy. Soc. London,* **286A,** 125–181.

——, 1987: Current and temperature variability on the continental slope. *Philos. Trans. Roy. Soc. London,* **323A,** 471–517.

——, 1992: Thermal fronts caused by internal gravity waves reflecting from a slope. *J. Phys. Oceanogr.,* **22,** 105–108.

——, P. Hall, and M. White, 1990: The variability of mixing at the continental slope. *Philos. Trans. Roy. Soc. London,* **331A,** 183–194.

Toole, J. M., R. W. Schmitt, K. L. Polzin, and E. Kunze, 1997: Fine- and microstructure evidence of boundary mixing above the flanks of Fieberling Guyot. *J. Geophys. Res.,* **102,** 947–959.

Wijesekera, H. W., and T. M. Dillon, 1997: Shannon energy as an indicator of age for turbulent overturns in the oceanic thermocline. *J. Geophys. Res.,* **102,** 3279–3291.